Smart Structures and Systems, *Vol. 32, No. 6 (2023) 383-391*
https://doi.org/10.12989/sss.2023.32.6.383

Broadband energy harvester for varied tram vibration frequency using 2-DOF mass-spring-damper system

Hamza Umar [1a], Christopher Mullen [1b], Soobum Lee*[1], Jaeyun Lee [2c] and Jaehoon Kim [3d]

[1] *Department of Mechanical Engineering, University of Maryland Baltimore County, 21250 Hilltop circle, Baltimore, MD 21250, USA*
[2] *CORECHIPS Co., Ltd., 33, Omokcheon-ro 132beon-gil, Gwonseon-gu, Suwon-si, Gyeonggi-do, Republic of Korea, Republic of Korea*
[3] *Korea Railroad Research Institute, 176, Cheoldobangmulgwan-ro, Uiwang-si, Gyeonggi-do, Republic of Korea*

(*Received October 31, 2023, Revised November 9, 2023, Accepted November 21, 2023*)

Abstract. Energy harvesting in trams may become a prevalent source of passive energy generation due to the high density of vibrational energy, and this may help power structural health monitoring systems for the trams. This paper presents a broadband vibrational energy harvesting device design that utilizes a varied frequency from a tram vehicle using a 2 DOF vibrational system combined with electromagnetic energy conversion. This paper will demonstrate stepwise optimization processes to determine mechanical parameters for frequency tuning to adjust to the trams' operational conditions, and electromagnetic parameters for the whole system design to maximize power output. The initial optimization will determine 5 important design parameters in a 2 DOF vibrational system, namely the masses (m_1, m_2 (and spring constants (k_1, k_2, k_3). The second step will use these parameters as initial guesses for the second optimization which will maintain the ratios of these parameters and present electrical parameters to maximize the power output from this system. The obtained values indicated a successful demonstration of design optimization as the average power generated increased from 1.475 mW to 17.44 mW (around 12 times).

Keywords: 2-DOF vibration system; broadband energy harvesting; design optimization; electromagnetic; tram vibration

1. Introduction

In recent years, energy harvesting has gained attention as a sustainable energy alternative for various applications where a remote power source is required. These include piezoelectric energy harvesting (Lu *et al*. 2022), thermo-electric energy harvesting (Dalala 2016), and photovoltaic energy harvesting (Kim *et al*. 2022). Generally, the goal of energy harvesting is to reduce the reliance on external energy sources like batteries. Since the power produced by these sources is not significantly high in many cases, this is used to power sensors with the purpose of early damage detection (Park *et al*. 2008). With the help of an energy harvesting system, these sensors can be autonomously powered for a long time without the need for battery replacement. Among the various applications of energy harvesting, monitoring sensors for railway systems have gained serious attraction, where rapid advances in structural health monitoring systems (SHM) enable the use of autonomous systems for monitoring railroad cabins and infrastructures (Davidson and Mo 2014).

Higher level of energy harvesting is expected from railroad systems because of the relatively high density of vibrational energy and noise, and one can realize a practical self-powering monitoring system wherever a battery-powered solution is hard to implement inside/outside of the cabin. Qi *et al*. (2022) explained that vibrational energy harvesting mechanisms can be broken down into single-degree-of-freedom systems and multiple-degree-of-freedom systems – the paper also reviewed vibration energy harvesting in railways and explained that two-degree-of-freedom systems can broaden the energy harvesting frequency and may have better overall stability in relation to external components connected to the vibration system. Considering varied frequency behavior in the railroad systems, the focus of this study will be a two-degree-of-freedom energy harvesting device combined with an electromagnetic energy conversion principle. Considering the harsh vibrational environment in railroad operation, electromagnetic harvesters can accommodate a durable solution rather than piezoelectric ones. Another research paper implemented a two-degree-of-freedom gravitational energy harvester using gravity as a restorative force and an electromagnetic harvesting system to produce energy, with different mass configurations were tested to find the best configuration optimizing power output, frequency bandwidth and overall performances (Monaco and Russo 2023). Similarly, Burrow and Penrose (2014) tested a two-degree-of-freedom mass-spring-damper system using a single electromagnetic transducer and demonstrated that higher-order devices have a significant advantage over single-degree-of-freedom systems in terms of being able to harvest energy at two frequencies simultaneously. Incidentally, Yu *et al*. (2021) used three magnets in the

*Corresponding author, Ph.D., Associate Professor,
E-mail: sblee@umbc.edu
[a] M.S., E-mail: hamzau1@umbc.edu
[b] Ph.D. Student, E-mail: mullen1@umbc.edu
[c] Principal Researcher, E-mail: jylee@corechips.co.kr
[d] Principal Researcher, E-mail: lapin95@krri.re.kr

ISSN: 1738-1584 (Print), 1738-1991 (Online)

electromagnetic coupling of a novel bistable two-degree-of-freedom electromagnetic energy harvester which showed two resonance frequencies and increased the working bandwidth of the harvester. Lee *et al*. (2009) implemented a two-degree-of-freedom energy harvester utilizing HVAC system vibration to power a wireless temperature sensor.

It is also important to note that in the realm of energy harvesting from railway systems, there may be differences in peak environmental frequencies due to the difference in the operating speeds of the trains themselves. To elaborate, Ung *et al*. (2015) used the relative motion between a magnet and a conductive coil in a heavy haul railcar application to harvest energy by tuning dominant frequencies of the host structure with resonance frequencies, with peak power outputs 212 mW and 218 mW at 6.5 Hz and 14.5 Hz respectively. On the other hand, Perez *et al*. (2020) focused on energy harvesting from a linear tram application where the average electrical output was 6.5 mW at resonance frequencies 25.7 Hz and 62.6 Hz, which are much higher. This is due to the difference in operating speed of the vehicles which naturally increases the oscillatory motion frequency.

For this study, the railway system used to harvest energy is a tram that operates relatively at low speeds (~ 50 km/h). The peak environmental frequency varies according to different operational conditions that should be considered in the design process of the harvester layout. The contents of this study will include an initial optimization of design parameters such as multiple mass and spring constants based on the frequency band constraints. These design parameters will then be implemented in a two-degree-of-freedom mass-spring-damper analysis model coupled with the electromagnetic energy conversion process (Kim 2021). Lastly, there will be an additional optimization performed and the parameters to maximize the expected average power within a specified frequency band with the corresponding mass and displacement constraints for design compactness. This work can contribute to practically power a sensor network with the purpose of structural health monitoring of the railway system to improve the longevity of the railway system and prevent any unexpected structural failures through early detection.

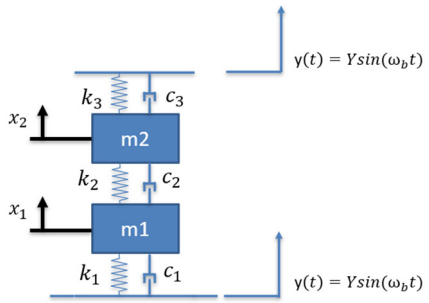

Fig. 1 Two-degree-of-freedom mass-spring-damper system with base excitation

2. Degree-of-freedom vibrational system: Equations of motion

The modeling of a two-degree-of-freedom harvesting system is explained in this section. It is important to note that this system has a closed end and the base excitation is applied from the upper and lower ends simultaneously as illustrated in Fig. 1. This layout has an advantage compared to the open-end design (no spring constant connected to mass 2 on upper end) considering a harsh railroad operational environment – a more reliable and durable component alignment is possible because of the supported ends on both sides. This layout can accommodate frequency tuning between the first and second mode frequencies and enable broadband harvesting (more details in Section 4 and 5).

Based on Fig. 1, the equations of motion can be analyzed using the free-body-diagram (Fig. 2) that shows the multiple spring/damping force terms.

Using the free body diagram analysis, one can obtain the following equations of motion, with Eq. (1) describing the displacement of m_1 where a magnet will be placed later and Eq. (2) describing the displacement of m_2. Eq. (3) describes the base excitation, which uses Y as the amplitude of the forced vibration and ω_b as the forced frequency in radian/s.

$$m_1\ddot{x}_1 + c_1(\dot{x}_1 - \dot{y}) + k_1(x_1 - y) + c_2(\dot{x}_1 - \dot{x}_2) + k_2(x_1 - x_2) = 0 \quad (1)$$

$$m_2\ddot{x}_2 + c_3(\dot{x}_2 - \dot{y}) + k_3(x_2 - y) + c_2(\dot{x}_2 - \dot{x}_1) + k_2(x_2 - x_1) = 0 \quad (2)$$

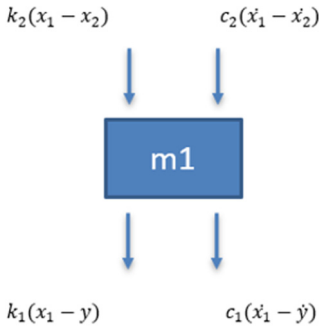

(a) Mass 1

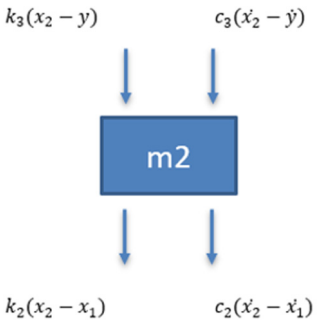

(b) Mass 2

Fig. 2 Derivation of equations of motion for two-degree-of-freedom system

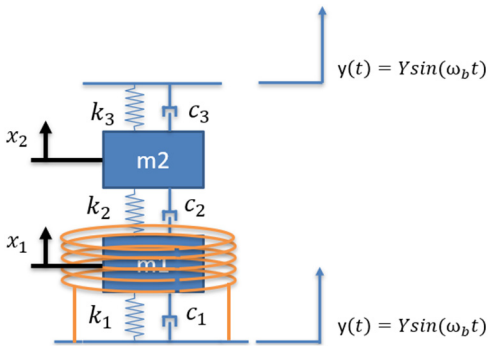

Fig. 3 Electromagnetic energy inducer design for two-degree-of-freedom mass-spring-damper system with coils (yellow)

$$y(t) = Ysin(\omega_b t), \;\; \dot{y}(t) = \omega_b Ycos(\omega_b t) \tag{3}$$

1.1 Incorporating induction into 2-degree-of-freedom vibrational system

An electromagnetic energy harvesting analysis is enabled by incorporating the voltage (current) induction term in a coil winding due to the change in magnetic flux density by a magnet attached to m_1, as shown in Fig. 3 where m_2 takes the role of frequency adjustment and does not have the coil around it.

The magnetic mass (m_1) will be displaced axially while a coil of wire arranged on the outside of the m_1 remains stationary. The magnet is polarized axially (or along the *y*-axis). Then, the system of coupled equations for the two-degree-of-freedom system is modified to include the interaction between the mechanical displacement of m_1 and the electrical power generation. Eq. (1) can be replaced by the following two equations

$$\begin{aligned} &m_1\ddot{x_1} + c_1(\dot{x_1} - \dot{y}) + k_1(x_1 - y) \\ &+c_2(\dot{x_1} - \dot{x_2}) + k_2(x_1 - x_2) + NlB_r i = 0 \end{aligned} \tag{4}$$

$$\frac{di}{dt} = -\frac{R + R_c}{L} i + \frac{1}{L} V_s(t) \tag{5}$$

In Eq. (4), the physical movement of mass m_1 and m_2 (x_1 and x_2) interact with the coil, and the relative displacement between the magnet (x_1) and the coil will result in electromagnetic current induction (i) which is related to the Lorentz force ($NlB_r i$), a function of the number of coil winding turns (N) with its averaged one turn length (l), and the magnetic flux density in the direction perpendicular to the surface of the magnet (B_r). Eq. (5) describes the time-varying current and voltage that are induced by the changing magnetic field from the physical movement of the mass, where R is load resistance, R_c is coil resistance, and L is coil inductance. Coil resistance is calculated using Eq. (6) formulated with the resistivity of copper wire (ρ), the total length of the wire ($l_w \approx Nl$), and the cross-sectional area of the copper wire (A_w) as

$$R_c = \frac{\rho l_w}{A_w} \tag{6}$$

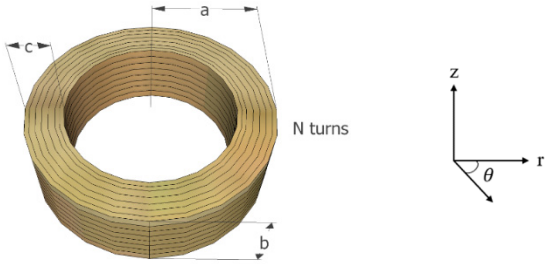

Fig. 4 Parameters in a coil winding for inductance calculation

The coil inductance L is calculated in Eq. (7) in units of micro-Henries (μH), using the geometric parameters (*a*, *b*, *c*) in Fig. 4 (Wheeler 1928).

$$L = \frac{31.6N^2(a-c)^2}{6(a-c) + 9b + 10c} \tag{7}$$

An important factor of electromagnetic energy harvesting is determining the magnetic flux density B_r around a magnet as a part of m_1 (Mullen and Lee 2016, Nezami *et al.* 2018). In this work the approximation of magnetic flux density is analyzed in two distinct paths: parallel to the magnet's lateral surface (along the *y*-axis) and normal to the magnet's lateral surface (along the *r*-axis). Along the *y*-axis, the magnetic flux density is the highest close to N (positive) and S (negative) poles, and it rapidly changes the sign between the poles. As it is distanced from the magnet, the magnetic flux density gradually reduces. Along the *r*-axis, on the other hand, the waveform along the *y*-axis is maintained, but the flux density decays exponentially as distanced far from the magnet. The details about the magnetic flux density modeling are described later in Section 3.

Eq. (2) and Eq. (4) are written in the following way to be integrated into the Simulink model, with Eq. (8) representing the acceleration of m_1 and Eq. (9) representing the acceleration of mass 2. Eq. (5) can be used as is in the Simulink model.

$$\begin{aligned} \ddot{x_1} = \frac{1}{m_1}(&-\dot{x_1}c_1 - k_1x_1 - c_2(\dot{x_1} - \dot{x_2}) - k_2(x_1 - x_2) \\ &+ NlB_r i + c_1 Y\cos(\omega_b t) \\ &+ k_1 Ysin(\omega_b t)) \end{aligned} \tag{8}$$

$$\begin{aligned} \ddot{x_2} = \frac{1}{m_2}(&-c_3\dot{x_2} - k_3x_2 - c_2(\dot{x_2} - \dot{x_1}) - k_2(x_2 - x_1) \\ &+ c_3 Y\cos(\omega_b t) + k_3 Ysin(\omega_b t)) \end{aligned} \tag{9}$$

A visual representation of the Simulink model is shown in Fig. 5, with part 1 and 2 describing the coupled mechanical system of m_2 and m_1, respectively, and part 3 showing the coupled mechanical and electrical components of the code. Eq. (8) takes the electrical component, and the two subsystems in the block diagram (part 3) describe the interaction terms: NlB_r/m and V_s/L.

In Eq. (8), the term NlB_r/m is the coupled term, where the current generated in Eq. (5) interacts with Eq. (8) and acts as an electrical damping term. The term V_s/L on the

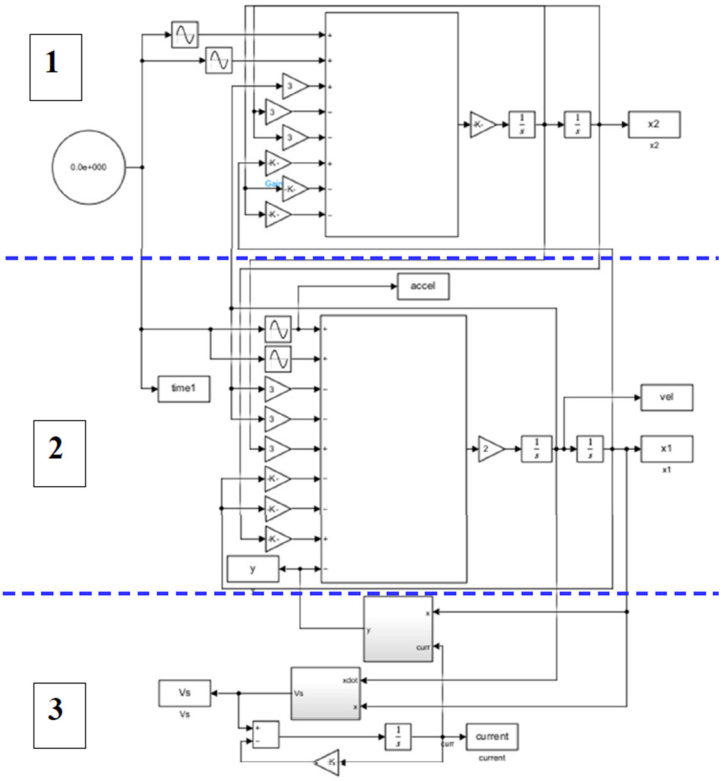

Fig. 5 Two-degree-of-freedom mass-spring-damper system in represented in Simulink

right side of Eq. (5) describes how the voltage generated from the movement of the physical system is involved in the induced current. Inside of subsystems in part 3, the voltage is calculated by integrating the voltage for each turn of the wire considering the location of each turn of the coil and the magnetic flux density distribution (Roundy and Takahashi 2013).

3. Experimental verification with one-degree-of-freedom electromagnetic energy harvester

This section verifies the coupled equations using a one-degree-of-freedom electromagnetic energy harvester product (Mullen 2017). A commercial electromagnetic harvester, nPower Personal Energy Generator (PEG, REI Item #849998), is purchased and the performance is measured. Inside of the protective case is housed one permanent magnet and a single coil of wire which are encased in a transparent cylinder. The magnet is supported by two springs from both ends of the cylinder. To retrieve experimental data from the PEG, the generator is fixed to a shaker (Labworks Inc, Model ET-126B-4) as shown in Fig. 6. There are electronics attached to the coil that manage the power coming out of the energy harvester and send the power to charge an onboard 2000 mAh lithium-ion battery. For this research, the circuitry and battery are removed, and the two wires from the coil are directly connected to the SCB-68A connector block for DAQ devices. In this way, the open-source voltage is measured. An accelerometer is attached to the shaker to acquire the input acceleration data. A known frequency is sent from the Wavetek Voltage

Fig. 6 nPower PEG as sold (left) and with protective case removed and mounted on a shaker to retrieve experimental data (right)

Controlled Signal Generator Model 19 to the shaker, and the amplitude of the vibration is measured by capturing video footage of a ruler next to the vibration and then freezing the frame to verify the values.

The governing equations that describe the nPower PEG can be obtained from Eq. (5) and Eq. (8) with several parameters set as zero (k_2, c_2). The open circuit voltage can be measured by setting $R = \infty$ (10^8 Ω chosen).

The values for the magnetic flux density (B_r) were determined by taking measurements using a Bell-5170 Gauss Meter. From the measured data, the magnetic density flux density can be curve fitted as a function of vertical (y) and radial (r) locations from the magnet surface as

Table 1 nPower PEG properties

Variable	Symbol	Value	Units
Mass	m	0.14	kg
Spring stiffness	k	22.89	N/m
Damping ratio	ζ	0.048	
Number of turns	N	3,814	
Wire Diameter	d	0.000127	m
Coil resistivity	ρ	1.724E-08	Ω m
Maximum flux density	B_{max}	0.1558	T
Decaying constant	α	105.7	
Flux fitting parameters	b_k	0.4590, 0.7757, -0.0153	
	c_k	157.7, 133.3, 89.97	
Inductance	L	0.28	H
Frequency	f	1.88	Hz

$$B_r\big(y, r(i)\big) = B_{max} e^{-\alpha r(i)} \times \sum_{k=1}^{3} e^{-(b_k + c_k(y))^2} \qquad (10)$$

where B_{max} is the maximum magnetic flux density on the pole surface of the magnet, and α is a constant to indicate exponentially decaying magnetic flux density, and i is the index of coil winding layer. The other parameters (b_k and c_k) are used to describe the changed waveform of the magnetic flux density along y-axis. In the magnetic flux density of the nPower PEG (Fig. 6) one can observe that as the distance from the surface of the magnet increases, the strength of the magnetic field decreases (gray dashed line in Fig. 7) as expressed by $e^{-\alpha r}$ term in Eq. 10. The flux density resembles a sine wave near the surface of the magnet (red dashed line in Fig. 7) and it is curve fitted using the sum of three exponential functions in Eq. (10). The curve fitted parameters are found as shown in Table 1. The gap between the magnet surface to the coil is set as 1.3 mm, and the coil thread diameter chosen as 0.127 mm (36 AWG). The spring constant and the damping ratio are experimentally measured.

The voltage results of the experimental data are shown overlaid on the simulation data in Fig. 8. The excitation

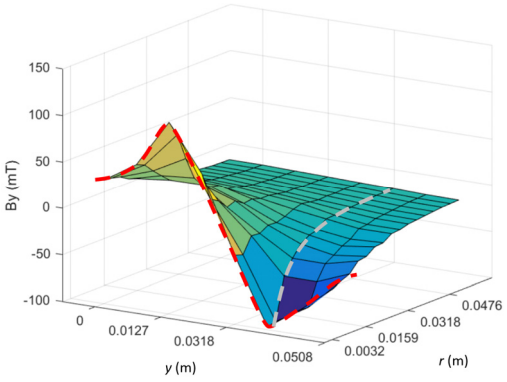

Fig. 7 Flux density parallel to lateral surface on y-axis (red) and normal to lateral surface on r-axis flux (gray)

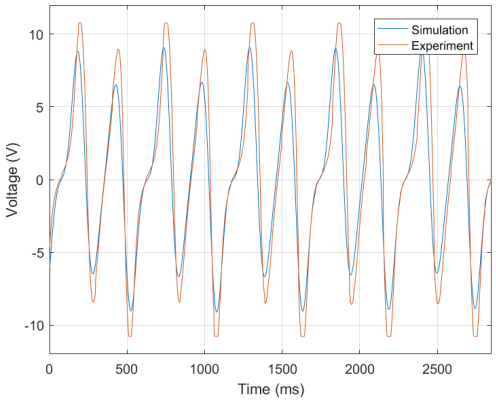

Fig. 8 Comparison of nPower PEG experimental data with simulation data

frequency is 1.88 Hz with a measured peak to peak amplitude of 6.35 mm that corresponds to the excitation acceleration of 0.44 m/s^2.

One can observe that the waveforms are identical but a slight difference in the maximum voltage magnitude. This is due to the sensitivity of the voltage magnitude with respect to the input displacement that is hard to control in a precise manner. In addition, there might be measurement error on magnetic flux density and the gap between magnet and coil. The current waveform is not perfectly symmetric and has some inflections because of the eccentricity of moving magnet (e.g., not perfectly centered with the coil at steady state) as well as asymmetric spring constants. However, both voltage waveforms identically show two cycles within one mechanical vibration cycle (1/1.88 = 0.53 seconds). The current sign changes according to the time rate of the magnetic flux around the coil. That is, the current is zero and changes its sign either when (1) the mechanical velocity becomes zero (at positive/negative peaks) or (2) the induced current is all canceled because the flux density rate is symmetric. This results in a doubled frequency of current signal (3.76 Hz) compared to the displacement frequency. It is concluded the simulation model is reliable to use for design purposes.

4. Design optimization

4.1 Tram vibration: Measuring vibration conditions

This study considers real operational conditions of a tram system tested in Korea Railroad Research Institute (KRRI) test rail. The tram is operated at a velocity range max 50 km/h. An ICP type wired sensors were used to measure the real time vibration signal on the bogie frame. The tram is tested to accelerate/decelerate in forward/backward directions, and it is found that the frequency for the maximum vibration (acceleration) varies according to the operational condition. Table 2 summarizes the vibration condition measured. The vibration level is higher when the tram cabin is in full capacity and the main frequency range is observed around 100 Hz. In the design process, we focus on broadband harvester design from 95 to 105 Hz and

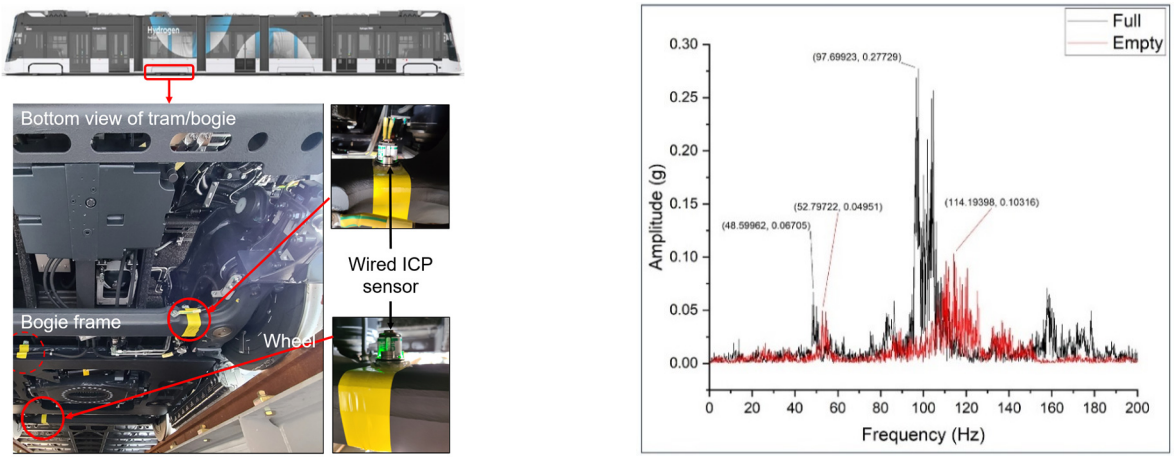

Fig. 9 Measuring tram vibration conditions

Table 2 Measured vibration condition (s) from tram system

Operational speed (km/h)	Frequency (Hz)	Input acceleration
50	95~105	0.2 g (1.96 m/s^2)

assume the input acceleration level to identical in each case as 0.2 g.

To realize an optimal design for this study, understanding the design constraints and the limitations of the design parameters can help us determine reasonable initial guesses for design parameters to use for power generation. As mentioned earlier, this study is to realize energy harvesting from a two-degree-of-freedom mass-spring-damper system, and it is important to focus on the behavior of the system in terms of the first two natural frequencies.

This study will take the step-wise design optimization approaches to find out: (1) mechanical parameters to realize the broadband vibration characteristic, and (2) the corresponding electromagnetic system parameters for power maximization. The first step is to perform frequency tuning to locate the first two natural frequencies within the tram operational frequency band, and the second step does the mechanical parameter tuning coupled with the electromagnetic parameters to maximize the power.

4.2 Design optimization: Frequency tuning

In the first step, the goal is to minimize the mass of the prototype which will eventually be manufactured with the design constraint as the first two resonance frequencies to locate within the frequency range of tram operation. Mass minimization is desired to realize a lightweight harvester, and the frequency constraint is important to enable broadband vibration energy harvesting – to generate significant power regardless of changed excitation frequency. The objective function, along with the constraints can be defined as follows

$$\begin{aligned} &\text{find} \quad m_1, m_2, k_1, k_2, k_3 \quad \text{to:} \quad \min m_1 + m_2 \\ &f_e - \Delta f \le f_1 \qquad f_2 \le f_e + \Delta f \end{aligned} \tag{11}$$

where f_e is the target frequency (100 Hz), Δf is the frequency tolerance (5 Hz), and f_1 and f_2 are the first two natural frequencies that are derived as a function of system masses and springs (Meirovitch 2001). X_1 is the maximum vibrational amplitude of m_1 in the excitation frequency band $[f_e - \Delta f, f_e + \Delta f]$ when the excitation force F_0 is set temporarily as 1 N.

The optimization process involves a multiparameter objective function subject to non-linear constraints, which can be performed using the 'fmincon' function in MATLAB. It is noted that 'fmincon' utilizes a gradient based optimization algorithm, and the result may be a local optimum dependent on the initial guess of the design parameters. To avoid it, this study performs a normalization process with the design parameters between 1 to 5 for 5 design parameters (5^5 = 3125 combinations) like a 5-level full factorial design, and the same number of optimization studies are conducted.

4.3 Design optimization: Power maximization

The second step of optimization will determine the whole system parameters to maximize the power out of the frequency band of interest, or

$$\begin{aligned} &\text{find} \quad x_c, c_i, N_t, R_o \quad \text{to:} \\ &\max P_{ave} \; at \; [f_e - \Delta f, f_e + \Delta f] \\ &s.t. \quad m_1 + m_2 \le m_{tot} \\ &X_1 \le d_0, \qquad X_2 \le d_0 \\ &f_e = 100\,Hz, \quad \Delta f = 5Hz \end{aligned} \tag{12}$$

where x_c is the scaling factor for the mechanical parameters found in the first step (m_1, m_2, k_1, k_2, k_3). By keeping the ratio between these parameters, one can maintain the two natural frequencies. c_i is the damping coefficient, N_t is the number of coil winding layers, and R_o is the external load to measure the power. For target frequency f_e = 100 Hz, the excitation frequency is assumed to vary between 95 Hz and 105 Hz, and the averaged power is evaluated in this frequency band based on the uniform acceleration at 0.2 g. For design compactness, the sum of the mass is constrained to be less than m_{tot} (= 0.7kg), and both displacement amplitudes are constrained to be less than d_0 = 5 mm.

The broadband power is evaluated as

$$P_{ave} = \frac{\int_{f_t-\Delta f}^{f_t+\Delta f} P(f)df}{2\Delta f} \quad (13)$$

where P is the power at a specific frequency f. This second step of optimization considers several initial guesses as figured out in Table 3. For design efficiency, we simulate time response within the frequency band with 1 Hz increment (95, 96, … 105 Hz) and the output power is numerically integrated. Total simulation time is set as 1.2 seconds.

Considering the allowed device size and mass values under a tram cabin, a magnet is chosen to have a larger diameter than the one-degree-of-freedom study. Two coin neodymium magnets (DY04-N52, diameter = 50.8 mm) are stacked to realize the total thickness is 12.7 mm. The maximum flux density (B_{max}) and the exponential decay constant (α) are assumed identical to the one in the one-degree-of-freedom study. The coil winding dimension is determined to accommodate a free vibration of m_1 inside the coil winding. The gap between the magnet surface to the coil is set as 1.3 mm (the inner diameter = 53.4 mm), and the same coil thread diameter is used as Section 3 (0.127 mm or 36 AWG). The number of coil winding layers (N_l) and the external load to measure the power (R_o) will be handled as additional design parameters.

Table 3 Step 1 result – for a target frequency of 100 Hz

m_i (kg)	k_i (kN/m)	f_i (Hz)
0.602, 0.076	239.523, 3.937, 25.513	97.67, 102.73
0.404, 0.126	161.926, 4.139, 44.877	97.86, 103.30
0.505, 0.126	201.281, 4.566, 44.493	97.81, 102.96

Table 4 Step 2 result – for a target frequency of 100 Hz

m_i (kg)	c_i (Ns/m)	k_i (kN/m)	max(x_i) (mm)	P_{avg} (mW)
0.257, 0.032	0.522, 4.442, 0.500	102.4, 1.683, 10.912	3.033	17.44
0.146, 0.046	0.500, 5.000, 0.500	58.521, 1.496, 16.219	2.350	5.835
0.198, 0.049	0.5025, 4.382, 0.500	78.800, 1.788, 17.419	2.640	8.114

5. Results

The first step of the optimization process generated the following values (Table 3) for the target frequency around 100 Hz. These values are used for the second optimization study that considers both mechanical and electrical parameters for power maximization.

These values are used for the second optimization study that considers both mechanical and electrical parameters for power maximization. Table 4 summarizes the design results. The external resistor and the number of coil layers are found as R_0 = 5.23 kΩ and N_t = 70 (the total number of turns = 13.6 k). All the designs satisfy the mass and displacement constraints. Among three designs, the first design is found to generate maximum power.

For the first design, the displacement and power profiles are presented in Fig. 10 as functions of frequency. One can observe the first step of design clearly demonstrates the first two resonance frequencies within the operational frequency band. However, in the second step the system parameters evolve to maximize the power and the bimodal behavior disappears. The underlying reasons for this are most likely because of the magnification of the intermediate damping constant (c_2(; the second optimization increases the magnitude of the damping constant so the system appears to have lost its bimodal characteristics, but in principle this should still be within the broadband energy harvesting range. It is noted that the damping coefficients before the second optimization step are c_i = 1.0 Ns/m, i = 1,2,3, and they evolve to maximize the area under the power profile. Through the second step optimization, the average power is increased from 1.475 mW (blue line) to 17.44 mW (red dot-dashed line) which is around 12 times increase. It is noted that the average power in higher acceleration band – [99 101] Hz – reaches to 61.13 mW.

The time histories of displacement (x_1) and the current at excitation frequency 100 Hz are displayed in Fig. 11. Once the response reaches the steady state, the maximum

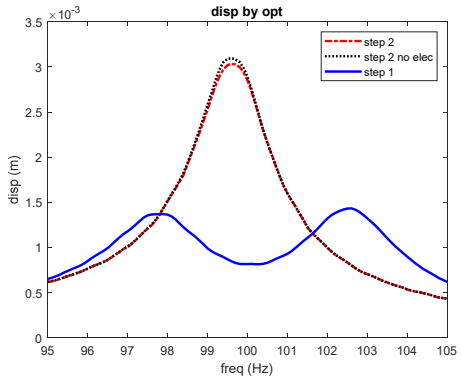

(a) Displacement profile

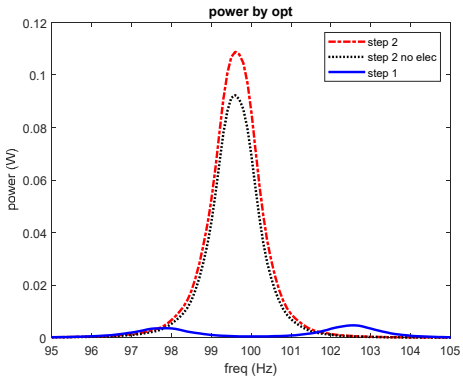

(b) Power profile

Fig. 10 Comparison of the performances before/after optimization

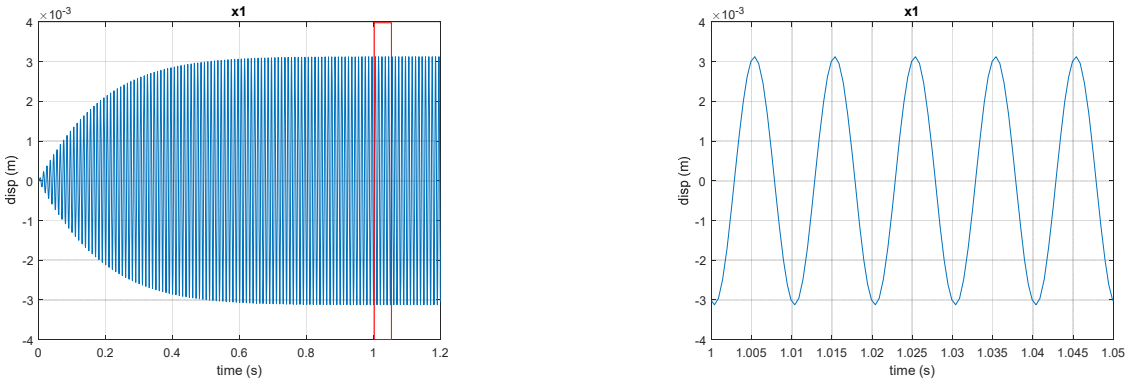

(a) Displacement (x_1) time history

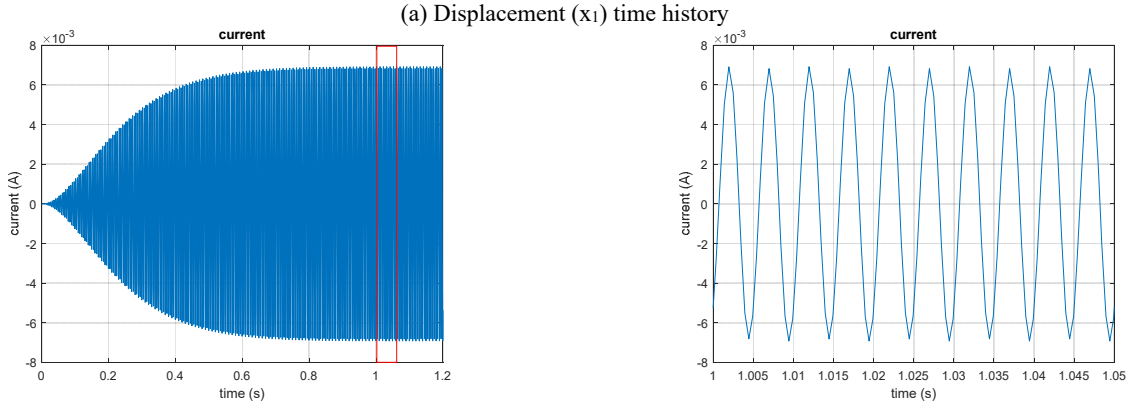

(b) Current time history

Fig. 11 Time history of displacement and current at 100 Hz

amplitudes for each measure are observed as 3.12 mm and 6.92 mA, respectively. A zoomed in view of each measure is also displayed from 1.0 to 1.05 second. The general electromagnetic current generation is well found as observed in Section 3– doubled frequency of current signal compared to the displacement frequency.

We could observe the damping coefficients are found differently at each connection, and c_2 (between m_1 and m_2) is found larger than the other two. This trend can be understood from the theorical background for tuned mass damper (or vibration absorber) (Meirovich 2001, Korenov and Reznikov 1994). An undamped vibration absorber can be designed by tuning m_2 and k_2 (and $k_3 = 0$) to match with the excitation frequency, or $f_e = 1/(2\pi)(k_2/m_2)^{0.5}$, but it only mitigates the amplitude at f_e and produces two other resonance frequencies (f_1 and f_2, $f_1 < f_e < f_2$). The intermediate damper (c_2) plays an important role in mitigating the excessive amplitudes at f_1 and f_2, and realizing the broadband characteristic. It is also interesting to observe that as c_2 approaches infinity, the system acts as a one-degree-of-freedom system with a single sharp peak response. This may also prompt the question of the necessity of a system with multiple degrees of freedom, but it is important to understand that the overall goal is still to make use of the broadband characteristic of a multiple-degree-of-freedom system – the power profile can be found broader if the objective function is defined to minimize the power variance at different frequencies. For practicability, we limited c_2 up to an implementable value (< 5 Ns/m) considering size limitation of m_2, but more in depth study is required about damping coefficient parameters.

A separate optimization was attempted without the electrical parameters (N_t, R_0) to investigate their effect only. Fig. 10 shows the design result from this optimization (black dotted line). Compared to the final design considering N_t and R_0 together (red dotted dash line), the vibrational amplitude is larger but the power level is smaller. It indicates that the coil winding and the external resistor are found to capture more vibrational energy to reduce mechanical amplitude (electrical damping) and increase the output power further.

6. Conclusions

This paper presented a two-degree-of-freedom vibrational energy harvester design with electromagnetic energy conversion considering varied frequency range from tram operational condition. Coupled equations for two mechanical vibrational displacement as well as electromagnetic current were derived, and a step-wise design optimization was performed for mechanical parameters for frequency tuning and additional electromagnetic parameters for the whole system design to maximize power output. In the first step to perform frequency tuning to locate the first two natural frequencies within the tram operational frequency band, enough initial guesses were attempted to avoid local optimality. Three possible designs were identified for the second step optimization where the mechanical parameters coupled with

the electromagnetic parameters are found to maximize the averaged power. As a result, the averaged power is increased from 1.475 to 17.44 mW indicating the successful implementation of optimization. This work is unique in terms of utilizing a two-degree-of-freedom vibrational system which has two resonance frequencies close to each other (within 5 Hz range), that can be efficiently tuned to realize a broadband energy harvesting for an excitation frequency that varies within a similar frequency band.

For future works, this project can evolve in many dimensions. The direct step is to design and manufacture a prototype that will include additional optimization processes for the power management circuit and energy storage to power wireless sensors. The physical damping coefficients can be realized using a commercial dashpot or by adjusting friction force between masses. The experimental will simulate a real world environment for the harvesting system by being mounted on a shaker which vibrates at the aforementioned frequency, and the power output will connect to a charging circuit which will store/use generated power for a sensor.

Additionally, a larger design space considering higher-order degree-of-freedom systems (with n masses) can be explored – as the number of masses increases, there is an increase in vibration modes which will lead to a higher frequency bandwidth for energy harvesting. This will also present the possibility of adding additional coils around the (magnetic) masses which will lead to a larger power output.

Acknowledgments

This work is supported by the Korea Agency for Infrastructure Technology Advancement (KAIA) grant funded by the Ministry of Land, Infrastructure and Transport (Grant 1615013220) and Korea Institute for Advancement of Technology (KIAT) grant funded by the Ministry of Trade, Industry and Energy (Project P0018646).

References

Burrow, S.G. and Penrose, L. (2014), "A 2 DOF vibration harvester for broadband and multifrequency harvesting using a single electro-magnetic transducer", *J. Phys*., **557**, p. 012031. https://doi.org/10.1088/1742-6596/557/1/012031

Dalala, Z.M. (2016), "Energy harvesting using thermoelectric generators", *Proceedings of 2016 IEEE International Energy Conference* (*ENERGYCON*), Leuven, Belgium, pp. 1-6. https://doi.org/10.1109/ENERGYCON.2016.7514088

Davidson, J. and Mo, C. (2014), "Recent advances in energy harvesting technologies for structural health monitoring applications", *Smart Mater. Res*., Article ID 410316, 14 p. https://doi.org/10.1155/2014/410316

Kim, J. (2021), "A study on the energy-harvesting device with a magnetic spring for improved durability in high-speed trains", *Micromachines* (*Basel*), **12**(7), 830. https://doi.org/10.3390/mi12070830

Kim, K.A., Bagci, F.S. and Dorsey, K.L. (2022), "Design considerations for photovoltaic energy harvesting in wearable devices", Sci. Rep. 12, 18143. https://doi.org/10.1038/s41598-022-22232-x

Korenov, B. and Reznikov, L. (1994), "Dynamic vibration absorbers: theory and technical applications", *Choice Reviews Online*, **31**(11), 31-6071. https://doi.org/10.5860/choice.31-6071

Lee, S., Youn, B.D. and Jung, B.C. (2009), "Robust segment-type energy harvester and its application to a wireless sensor", *Smart Mater. Struct*., **18**(9), 095021. https://doi.org/10.1088/0964-1726/18/9/095021

Lu, D., Li, Z., Hu, G., Zhou, B., Yang, Y. and Zhang, G. (2022), "Two-degree-of-freedom piezoelectric energy harvesting from vortex-induced vibration", *Micromachines*, **13**(11), 1936. https://doi.org/10.3390/mi13111936

Meirovitch, L. (2001), *Fundamentals of Vibrations*, McGraw-Hill, Boston, MA, USA.

Monaco, M.L. and Russo, C. (2023), "Design methodology of a two-degrees-of-freedom gravitational energy harvester", In: *IOP Conference Series*, **1275**(1), p. 012042. https://doi.org/10.1088/1757-899x/1275/1/012042

Mullen, C. (2017), "Design Optimization of an Electromagnetic Energy Harvester Backpack for Utilization of Human Walking Energy", Thesis.

Mullen, C. and Lee, S. (2016), "Optimization of an electromagnetic energy harvesting backpack under actual walking and running scenarios", *Proceedings of the ASME 2016 Conference on Smart Materials*, *Adaptive Structures and Intelligent Systems*, Stowe, VM, USA, September. https://doi.org/10.1115/SMASIS2016-9291

Nezami, S., Lee, S., Jin, J. and Kang, K. (2018), "Shape optimization of railroad vibration energy harvester for structural robustness and power generation performance", *Eng. Struct*., **173**, 460-471. https://doi.org/10.1016/j.engstruct.2018.07.011

Park, G., Rosing, T., Todd, M.D., Farrar, C.R. and Hodgkiss, W. (2008), "Energy harvesting for structural health monitoring sensor networks", *J. Infrastr. Syst*., **14**(1), 64-79. https://doi.org/10.1061/(ASCE)1076-0342(2008)14:1(64)

Perez, M., Chesné, S., Jean-Mistral, C., Billon, K., Augez, R. and Clerc, C. (2020), "A two degree-of-freedom linear vibration energy harvester for tram applications", *Mech. Syst. Signal Process*., **140**, 106657. https://doi.org/10.1016/j.ymssp.2020.106657

Qi, L., Pan, H., Pan, Y., Luo, D., Yan, J. and Zhang, Z. (2022), "A review of vibration energy harvesting in rail transportation field", *iScience*, **25**(3), 103849. https://doi.org/10.1016/j.isci.2022.103849

Roundy, S. and Takahashi, E. (2013), "A planar electromagnetic energy harvesting transducer using a multi-pole magnetic plate", *Sensors Actuators A*: *Phys*., **195**, 98-104. https://doi.org/10.1016/j.sna.2013.03.018

Ung, C., Moss, S.D. and Chiu, W.K. (2015), "Electromagnetic energy harvester using coupled oscillating system with 2-degree of freedom", *Proceedings of SPIE*, 94312C. https://doi.org/10.1117/12.2084416

Wheeler, H.A. (1928), "Simple inductance formulas for radio coils", *Proceedings of the Institute of Radio Engineers*, **16**(10), 1398-1400. https://doi.org/10.1109/JRPROC.1928.221309

Yu, N., Ma, H., Wu, C., Yu, G. and Yan, B. (2021), "Modeling and experimental investigation of a novel bistable two-degree-of-freedom electromagnetic energy harvester", *Mech. Syst. Signal Process*., **156**, 107608. https://doi.org/10.1016/j.ymssp.2021.107608